Volume 1 | Number 1 | Jan 2013 | Pages 1–100

Journal of
Materials Chemistry A

Materials for energy and sustainability
www.rsc.org/materialsA

ROYAL SOCIETY
OF CHEMISTRY

ROYAL SOCIETY
OF CHEMISTRY

www.rsc.org/materialsA

Journal Name

Dynamic Article Links ▶

ARTICLE TYPE

The Effect of Photoanode Structure on the Performances of Quantum-dot Sensitized Solar Cells: A Case Study of the Anatase TiO$_2$ Nanocrystals and Polydisperse Mesoporous Spheres Hybrid Photoanodes

₅ **Dapeng Wu,[b] Xiaojuan Shi,[c] Hui Dong,[a] Feng Zhu,[a] Kai Jiang,[b*] Dongsheng Xu,[a*] Xicheng Ai[c*] and Jianping Zhang[c]**

TiO$_2$ polydisperse mesoporous spheres (PMSs) and nanocrystals were selectively prepared *via* slightly
₁₀ altering the precursor dosage in a solvothermal reaction. Afterwards, the submicrometer sized PMSs and nanocrystals were adopted as sample materials to shed light on the effect of the photoanode structure over the performance of CdS/CdSe co-sensitized solar cells by comparing four types of photoanode structures: nanocrystal film, blend film, bilayer film and PMSs film. It was found that the bilayer photoanode could promote the harvesting of incident light by increasing both the CdS/CdSe QDs loading amount and the
₁₅ scattering effect. According to the transient photovoltage measurements, the carrier recombination at the TiO$_2$/electrolyte and FTO/electrolyte interfaces were substantially passivated in the bilayer cell. Moreover, a high electron diffusion rate of 142.0×10^{-9} m^2 s^{-1} was also obtained in the bilayer cell, indicating high photoelectrons collection efficiency in the film structure. Therefore, the bilayer cell can well integrate the structural advantages of the PMSs and nanocrystals, which contributes to a high
₂₀ conversion efficiency of 4.70 %, demonstrating a ~54 % and ~12 % improvement compared with the cells respectively derived from nanocrystal and PMSs.

Introduction

The ever increasing demand for clean, renewable and low-cost energy of the human society engendered the researches on
₂₅ developing the next-generation solar cells. Dye-sensitized solar cell (DSSC) is one of the most hot-pursuit configuration, the photovoltaic conversion efficiency (*PCE*) has already exceeded 13% by the persistent optimization of the working electrode, dyes, electrolyte and counter electrodes.[1-5] Recently, as an alternative to
₃₀ organic dyes, semiconductor quantum dots (QDs) with higher extinction coefficients and greater intrinsic dipole moments were studied for their high light-harvesting capability and longer stability.[6-10] Moreover, the semiconductor QDs exhibit attractive characteristics as sensitizers due to their tunable band gap by size
₃₅ control or allying to match the absorption spectrum with the sunlight spectral distribution.[11-14] In addition, the unique multiple exciton generation, the formation of more than one exciton upon the absorption of a single photon, is of great importance in QDs sensitized solar cells (QDSSCs), in which the thermodynamic
₄₀ photovoltaic conversion efficiency could be further pushed up to 44% from the current 31% of the Shockley−Queisser detailed balance limit.[15-18]
Therefore, QDSSCs have attracted significant attention as promising third-generation photovoltaic devices, which leads to
₄₅ the rapid increase of photovoltaic conversion efficiencies around 4−5% at 1 sun illumination (AM 1.5, 100 mW cm^{-2}) in the past two years. Impressively, record PCE of 5.4% with Mn-doped

QDSSC and 6.3% with panchromatic photon harvesting in Sb$_2$S$_3$-sensitized solar cells were demonstrated.[19,20] Most recently, a
₅₀ large varieties of narrow band semiconductors with border light response scale and higher extinction ratio were employed as the sensitizers in QDSSCs, such as CdSe, CdTe, PbS, Ag$_2$S, PbSe, and so on.[21-28] In addition, many research works were devoted to sophisticate the device configuration from different aspects such
₅₅ as the photoanode oxide matrix, QDs loading technique, counter electrodes and electrolytes.[29-35] The *PCE* of QDSSCs, however, still lags far behind than those of DSSCs, which mainly results from the incompatible band structural alignments between the sensitizers and the oxides photoanode matrix and the massive
₆₀ charge recombination taking place at the TiO$_2$/electrolyte, Ti/QDs and FTO/electrolyte interfaces.[36,37]
In a working QDSSC, the QDs are excited by incident light to generate electron−hole pairs. The electrons are subsequently injected into the TiO$_2$ conduction band, and then transported to
₆₅ the transparent conductive oxide electrode. On the other hand, the holes are injected into the hole-transporting electrolyte and finally reach to the counter electrode, where the oxidized counterpart of the redox system is reduced. Although the sandwiched QDSSCs structure shared a lot of working principles in common with the
₇₀ conventional DSSCs, there are still some elementary differences, which is essentially attributed to the remarkable distinction between QDs and conventional dyes both in intrinsic nature and fabrication technique.[38,39] Compared with Ru-polypyridine or organic dyes, the diameter of QDs is generally several
₇₅ nanometers, which are much greater than that of the dye

molecules. Therefore, the pores of the photoanode film are easier to be blocked by the large size QDs, especially when multiple layer QDs are formed in the loading process, which could directly prohibit the penetration of the electrolyte and decrease the re-generation of the oxidized QDs. In addition, large pore size distribution could also facilitate the loading process of the QDs and increase the QDs coverage, which is of great significance to promote the light harvesting and inhibit the recombination rate of the photogenerated carriers.[40,41] Moreover, different from the chemical bonds established at the dye/TiO_2 interface, semiconductor heterojunction were formed *via* the *in situ* growth process, which should be delicately controlled at low defect level to allow a high injection rate of the photoelectron.[42] Due to the high extinction ratio of the QDs, the surface area of the film may not be highly required compared with the DSSCs system, but, the scattering effect helping to harvest the incident light with longer wavelength is still necessary.[43] Previous work shows the thickness of additional scattering layer is of great influence on the cell performances.[44] To date, the commonly used porous TiO_2 structure generally inherited from the optimization of DSSC system. Therefore, when it comes to QDSSC, the photoanode structures should be redesigned to meet the requirement of the new system.

Herein, we presented a case study to shed light on the influence of the photoanode film structure on the performance of QDSSCs. Firstly, self-made TiO_2 nanocrystal and PMSs were selectively prepared *via* a solvothermal method by altering the peroxotitanium complex precursor dosage. Subsequently, these TiO_2 products were adopted to prepare four types of photoanode: nanocrystal film, blend film, bilayer film and PMS film. The photocurrent–photovoltage (*I–V*) characteristics shows the QDSSC deriving from the bilayer photoanode possess the best *PEC* of 4.70%, which indicates a ~54% increase compared with the conventional nanocrystal cell. Based on the investigation of the film structure, cell performance and the kinetic parameters of the photoelectron, the advantageous of the bilayer photoanode structure were interpreted in detail.

Experimental

Preparation of TiO_2 products: 12.5 mL tetrabutyl titanate (TBT) was slowly added into a mixture solution of 50 mL hydrogen peroxide (H_2O_2, 30 wt%) and 5 mL ammonia (NH_4OH, 26–28 wt%) dropwise in a 500 mL baker with continuously shaking. (**Caution**: great deal of heat was generated in the dissolving process, which could lead to the violent boiling of the liquid companied with the emission of unpleased smell.) Afterwards, cold distilled water was poured into the baker to yield a saffron yellow precursor solution with final volume of 200 mL. The precursor solution was filtered to remove the undissolved yellow bulks occasionally flouting on the solution. Then, 10 mL of this yellow precursor was extracted and transferred into a 50 mL Teflon container with additions of 10 mL distilled water and 20 mL absolute ethanol. The mixture was sealed tightly with a stainless jacket and heated at 180 ºC for 10 h. The final residue was centrifuged and washed with water and ethanol, respectively. Finally, the as-prepared sample was dried at 60 ºC for 2 h. In addition, the precursor dosage was adjusted to 5 mL to prepare the anatase nanocrystals.

Materials characterizations: The morphologies and structures of the products were characterized by field-emission scanning electron microscopy (FESEM, HITACHI, S4800), transmission electron microscopy (TEM, FEI Tecnai F30), X-ray powder diffraction (XRD, Rigaku D/max-2500 diffractometer with Cu Kα radiation, λ= 0.1542 nm, 40 kV, 100 mA) and Brunauer–Emmett–Teller (BET, Micrometrics ASAP 2010). Moreover, energy dispersive spectroscopy (EDS, Oxford, INCA MICSF+) was also used to characterize the film structure loaded with QDs.

Preparation of photoanode films: The paste was prepared by adding 10 wt% hydroxypropyl cellulose (Aldrich) into diethylene glycol under vigorous stirring in a 105 ºC oil bath for 5 h. Then, the as-prepared paste was added into the stock TiO_2 wet product and the mixture was stirred for about 2 h to obtain the homogeneous slurry. For the blend films, the nanocrystal and the PMSs products are mixed equally in weight. The bilayer film was constructed by the doctor-blade method through two-step calcination. Nanocrystal slurry was spread onto fluorine-doped tin oxide (FTO) glass substrate (TEC-8, LOF) with adhesive tape to control the film thickness. After dried in air, the film was heated up to 450 ºC at a rate of 5 ºC min^{-1} and maintained for 30 min. After calcination, another layer of PMSs slurry was deposited on the semi-transparent layer and annealed with the same heating profile. The single layer films: nanocrystal film, blend film and PMS film were prepared in similar processes. In addition, the active areas of the films are controlled at ~0.25 cm^2 by scratching off the excess film.

Fabrication of QDSSCs: A modified version of chemical bath deposition method was applied to load the CdS and CdSe QDs on the TiO_2 photoanode. For the deposition of the CdS QDs: an aqueous solution with the composition of 0.02 mM $CdCl_2$, 0.14 mM thiourea ,0.07 mM NH_4Cl and 0.23 mM ammonia with a final pH of ~9.0 in the chemical bath at 10 ºC for 1 hour. Afterwards, TiO_2/CdS films were immersed in an aqueous solution containing 0.026 mM $CdSO_4$, 0.04 mM $N(CH_2COONa)_3$ and 0.026 mM Na_2SeO_3 for 4.5 h in the same way. Both the QDs (CdS and CdSe) depositions films were washed with distilled water. For the ZnS passivation, all the films which after sensitization were deposited by twice dipping alternatively into 0.1 M $Zn(CH_3COO)_2$ and 0.1 M Na_2S solutions for 1 min per dip, rinsing with deionized water between dips. Cu_2S on brass was used as a counter electrode according to the literature. The CdS/CdSe QD-sensitized photoanodes and counter electrode were sandwiched to form the cell, which was separated by adhesive tape spacer (~60 μm in thickness).The electrolyte composed of 1 M Na_2S and 1 M S in deionized water was injected into the cell via capillarity.

Photovoltage measurements: Photocurrent–voltage (*I–V*) measurements were performed on a Keithley 4200 semiconductor characterization system using a simulated AM 1.5 sunlight with an output power of 100 mW cm^{-2} produced by a solar simulator (Newport 69911). The cells were placed 25 cm away from the light source and illuminated from the front side. Incident monochromatic photo-to-electron conversion efficiency (IPCE) was recorded on a Keithley 2000 source meter under the irradiation of a 150 W tungsten lamp with a 1/4 m monochromator (Spectral Product DK240). The optical diffusion reflection spectra and absorbance spectra were measured using a spectrophotometer (HITACHI U-4100).

Transient photoelectron dynamic measurements: Two light emitting diodes (LED 530 nm) were used as the bias light source to generate the steady voltages and the pulse excitation light source to produce transient signals. Light from these two LEDs was collected by two identical lens groups and imaged on the QDSSC surface with a spot size of 8 mm×8 mm. The bias light intensity could be adjusted from 1 μW to 60 μW by a DC regulated power supply to generate different steady open circuit voltages. The pulse light LED was driven by a self-made pulse amplifier and the excitation light intensity was set as 2 μJ per pulse with a duration of 50 μs. The photovoltage transients under
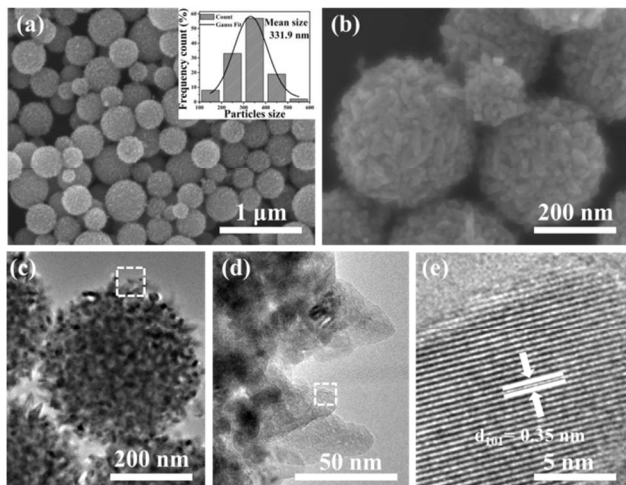
Fig. 1 the (a, b) SEM, (c-d) TEM and (e) HRTEM images of the as-prepared PMSs. The inset gives the corresponding diameter distribution histogram.

5 different steady bias voltages were directly recorded using an oscilloscope (Lecroy 64Xs) with an input resistance of 1 MΩ. The photocurrent transients under different bias voltages were recorded using an oscilloscope with an input resistance of 50 Ω and shunted with a 50 Ω series resistor. Moreover, a current 10 amplifier (Stanford Research Systems, SR445A) was also incorporated in front of the oscilloscope. The as-obtained photovoltage decay curves were fitted by Matlab 7.0 with an exponential function of $y=y_0 + A_1exp(-x/t_1) + A_2exp(-x/t_2)$, where y_0 is the baseline, A_1 and A_2 are the pre-exponential factors, t_1 and 15 t_2 are the time constants. Afterwards, the recombination lifetime (τ_r) and the collection time (τ_{col}) are calculated according to the equation $\tau=(A_1t_1 + A_2t_2)/(A_1 + A_2)$.

Results and Discussions

Fig. 1 a and **b** depict the PMSs prepared *via* a one-step 20 solvothermal method. The as-prepared products are in spherical shape and the inset diameter distribution histogram indicates the diameter of the product ranges from 100 to 600 nm, with an average size of 331.9 nm. Moreover, the zoom-in SEM image shows that the spheres are assemble from nano-sized spindles 25 about several nanometers in diameter and several tens of nanometer in length. Compared with the well-defined spheres with uniform diameter, The polydisperse product could increase the connection between the adjacent spheres, and lead to a better electron transport when used as photoanode materials.[45,46] In 30 addition, control experimental was carried out to reveal the grow mechanism of the as prepared PMSs. **Fig. S1 a** and **b** presents the SEM images of the intermediate products collected at 30 min. It is evident that polydisperse spheres were formed in the reaction with smooth surface. As it is demonstrated in our previous work, 35 in this reaction system, amorphous precursor spheres were firstly formed by the coordination between the Ti and carboxyl groups and the later cross link of the Ti contained complexes, which would function as a template to guide the in situ crystallization of the polydisperse spheres.[47,48] Compared with the intermediate 40 spheres, these crystallized PMSs have smaller size distributions, indicating the crystallization leads to diameter shrinkage of the intermediate products. The corresponding TEM image shows the as-prepared product processes mesoporous structures (**Fig. 1c**). Moreover, the sprout-like crystals at the surface of the sphere 45 exhibit sharp tips and spindle-like configuration (**Fig. 1d**). Furthermore, in the HRTEM image of the tip area of an
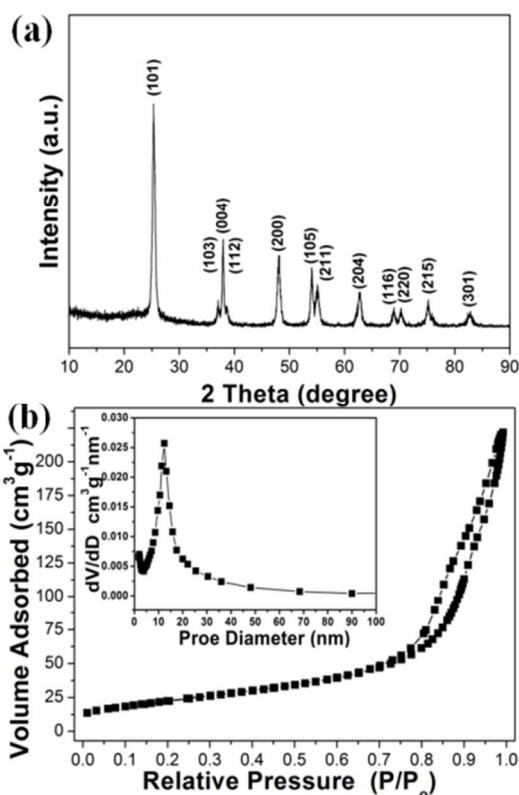

Fig. 2 (a) XRD pattern and (b) nitrogen adsorption isotherm of the polydisperse mesoporous spheres. The inset in (b) is the 50 corresponding pore size distribution curve.
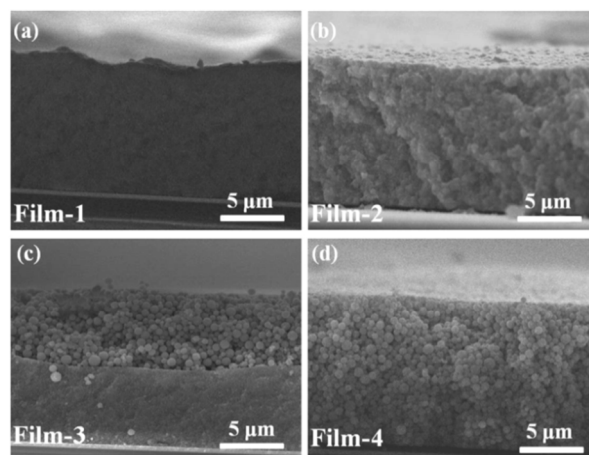

Fig. 3 the structure of four type photoanodes deriving from the different combination of the PMSs and the nanocrystals: (a) nanocrystal film (Film-1), (b) blend film (Film-2), (c) bilayer film 55 (Film-3) and (d) PMSs film (Film-4), the film thickness are all controlled at ~14 μm.

individual nanospindle, the well-defined lattice fringes with interplane spacing of 0.35 nm indicate the primary nanospindles are highly crystallized with anatase phase structure (**Fig. 1e**).[49] The 60 XRD pattern of the PMSs is presented in **Fig. 2a**, in which all the diffraction peaks can be indexed to anatase TiO_2 (JCPDS No.21-1271). The nitrogen adsorption isotherm, as-shown in **Fig. 2b**, exhibits a type-IV isotherm with H3-type hysteresis at high relative pressures, which confirms the existence of large pores in 65 this sample.[50,51] A narrow pore size distribution with a peak size of about 17 nm is observed in the pore-size distribution curve (the inset of **Fig. 2b**). Moreover, the Brunauer–Emmett–Teller (BET)
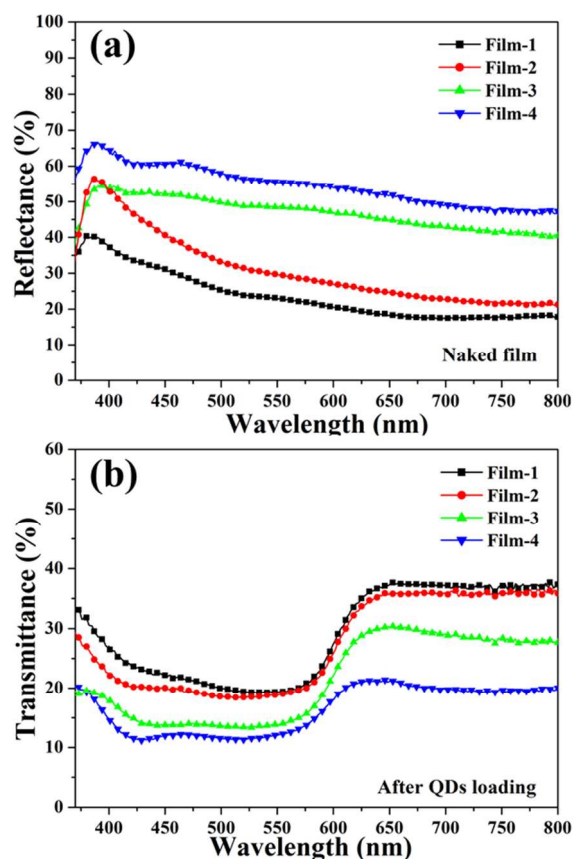
Fig. 4 (a) UV-Vis reflection spectra of the photoanode film, (b) the transmittance spectra of the photoanode film after QDs loading.

surface area of the sample is measured as ~82.2 m^2 g^{-1}. **Fig. S2a** shows the anatase nanocrystals prepared by simply reducing the precursor dosage in a similar preparation system. The as-prepared nanocrystals are about ~15 nm in average diameter, with BET surface area of ~89.3 m^2 g^{-1}. The corresponding XRD pattern (**Fig. S2b**) suggests the products exhibits well crystallized anatase structure. Moreover, it is obvious that the diffraction peaks belonging to (103), (004) and (112) are integrated together, indicating the broadening of the diffraction peaks due to the decreased particle size.[52]

The as-prepared polydisperse spheres and the nanocrystals were employed as raw materials to fabricated four types of photoanodes to study their structural influence on the performance in QDSSCs. **Fig. 3** shows the cross sections of the four photoanode films: (a) nanocrystal film, (b) blend film, (c) bilayer film and (d) PMS film, which are respectively denoted as Film-1, Film-2, Film-3 and Film-4.The film thickness are all controlled at ~14 μm, and the bilayer film composes of PMS and nanocrystal layers equal in thickness (~7 μm). **Fig. 4 a** presents the UV-Vis reflection spectra of the four photoanode films without QDs loading. Film-2 assembled from the mixture of nanocrystals and PMSs exhibits a similar reflectance behavior compared with Film-1, the reflectance value plummets in the visible and red region, indicating the high transmittance of low energy photons. Moreover, compared with Film-3, Film-4 possesses a better scattering effect because of the film are constructed by solely PMSs. Furthermore, characteristic photonic reflection peaks are observed in Film-4 and Film-3, which are in good agreement with the size dependent behavior of the light scattering effect.[53] **Figure 4b** depicts the transmittance spectrum of the photoanode after QDs loading. The transmittance in the
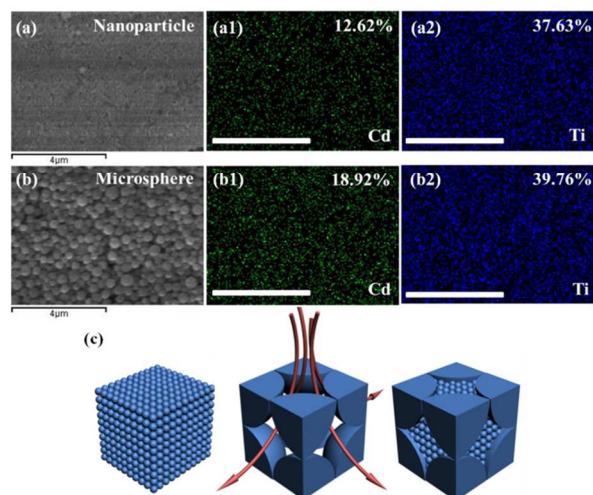

Fig. 5 the EDX mapping analysis of the (a) nanoparticle and (b) PMS films after QDs loading; (the element percentage composition are shown in massive ratio (wt%) and the scale bars are 4 μm), (c) illustration on the film structures.

region of 400-600 nm is associated the absorption of CdS/CdSe QDs, which reflects the loading amount in the photoanode.[54] Particularly, the peak at 400-500 nm region is related to absorption of CdS QDs and that at 550-650 nm region derives from the absorption of CdSe QDs. While, the curves at the region of 650-800 nm depend on the scattering effect of the films. Film-1 has the highest transmittance, suggesting the nanocrystal film is not a suitable candidate to promote the loading process of the QDs. Although the transmittance of Film-2 is slightly reduced, it is still much higher compared with Film-3 and Film-4. Moreover, Film-3 outperform Film-1 and Film-2 at both the 400-600 nm and 600-800 nm regions, which are respectively resulted from the high QDs loading amount and the improved scattering effect helping to trap low energy photons in the photoanode. Film-4 has the lowest transmittance in the whole wavelength, which implies a greater amount of the QDs with high coverage ratio was supposed to form on the PMSs film.

Moreover, the QDs loading difference could be further confirmed by the EDX mapping analysis. **Fig. 5 a and b** shows the element percentage composition (Cd, Ti) on the surface of Film-1 and Film-4 after QDs loading, the Cd/Ti ratio are 0.34/1 and 0.48/1 for the two films, indicating Film-4 has a much higher QDs loading amount, although the PMSs possess relative lower surface area. As shown in the illustration of **Fig. 5c**, the closely packed nanocrystals film cannot afford enough channels for the diffusion of the precursor solution, and the channels could be easily blocked by the ever growing QDs (the left side carton). The central image reveals the adjacent aggregated spheres leaves many voids unoccupied in the film structure, which could increase the diffusion cross section of the precursor solution. The QDs loading process accompanied with the continuous *in situ* consumption of the solute (the Cd^{2+} and the S^{2-} or Se^{2-} species) in the precursor solution, which would lead to a concentration gradient between the precursor solutions trapped in the film structure and the bulk reaction system. According to the Frick's first law, the diffusion rate of the solutes would increase proportionally to the diffusion cross section, if the diffusion coefficient and the concentration gradient are considered as constants. Therefore, in the PMSs film, the concentration gradient could be rapidly filled up due to the greater diffusion cross section, which could facilitate the QDs growth. As for Film-2, the mixed nanocrystals could fill the voids between the adjacent
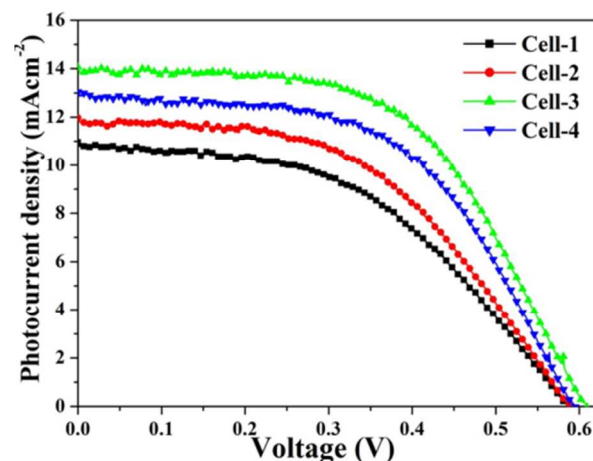
Fig. 6 *I–V* curves of the QDSSCs based on different photoanodes measured under one sun illumination (AM 1.5G, 100 mW cm^{-2}).
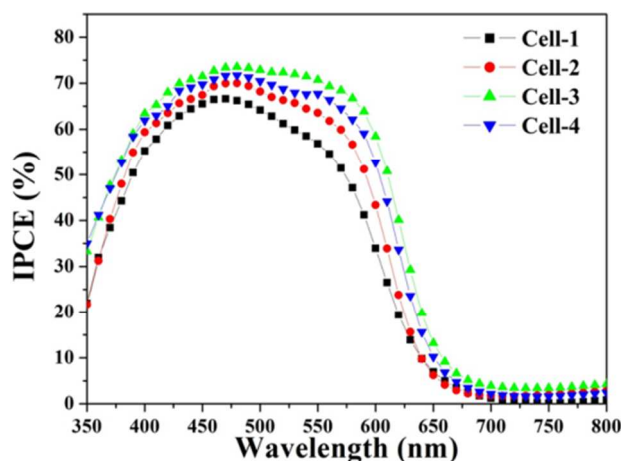
Fig. 7 Incident-photon-to-current conversion efficiency (IPCE) spectra of the as-prepared QDSSCs.

Tab. 1 Photovoltaic performance of QDSSCs derived from different photoanode structures (the active area for all the cells is ~0.25 cm^2)

Cells	J_{sc} / mA cm^{-2}	V_{oc} / mV	FF (%)	PCE (%)	Film thickness (μm)
Cell-1	10.96	588	47.3	3.05	~14
Cell-2	11.97	589	49.2	3.47	~14
Cell-3	14.06	608	55.0	4.70	~7+7
Cell-4	13.04	594	53.9	4.18	~14

spheres, in these sense, the mixed film could be considered as a nanoparticle film (the right side carton). Therefore, it could be 10 concluded that the PMSs film holds the structural priority in facilitating the QDs loading process and the pore structure of the film are much important than the surface area in facilitating the QDs loading process. [55,56]

The photocurrent–photovoltage (*I–V*) characteristics of the 15 QDSSCs based on the four photoanodes are shown in **Fig. 6** and the corresponding photovoltaic characteristics are summarized in **Tab. 1**. Compared with Cell-1, Cell-2 had an enhanced conversion efficiency of 3.47%, which was attributed to the increased short-circuit photocurrent density (J_{sc}) and filling factor 20 (*FF*). Meanwhile the open-circuit photovoltage (V_{oc}) of the QDSSCs remain almost unchanged. Cell-3, based on the bilayer photoanode, outperformed the other cells in all the list parameters: *FF* of 55%, V_{oc} of 608 mV and J_{sc} of 14.06 mA cm^{-2}, which leads to the highest PCE of 4.70%, indicating an ~54% 25 augment compared with the nanocrystal cell. Based on the optical test of the photoanode, the increased J_{sc} is estimated resulting from the high light capture ability of the photoanode. In addition, the high QDs loading amount also helped to improve the V_{oc} and *FF* of the cell, by building physical passivation layer at the 30 TiO$_2$/electrolyte interface. Cell-4 which derives from the PMSs photoanode was also tested. Although Cell-4 has higher QDs loading amount and greater scattering effect, the J_{sc} and V_{oc} was slightly decreased, which leads to a reduced PCE of 4.18 % compared with Cell-3.

35 **Fig. 7** shows the incident-photon-to-current conversion efficiency (IPCE) spectra in function of wavelength for the four QDSSCs. Due to the improved scattering effect and the high QDs loading amount, Cell-3 and Cell-4 demonstrated higher IPCE values. The absolute IPCE of Cell-3 was higher than the other cells in the 40 entire wavelength region, which was in good agreement with the corresponding high J_{sc}. In addition, compared with Cell-3, the characteristic peak at 500-650 nm is obviously clearer, which indicates the scattering effect in Cell-4 is more prominent. However, as it is demonstrated in Eqn. 1, the IPCE value of

45
$$IPCE = \eta_{lh} \times \eta_{inj} \times \eta_{col} \quad (Eqn.1)$$

DSSCs is determined by the light harvesting efficiency of the film (η_{lh}), the injection (η_{inj}) and collection efficiencies (η_{col}) of the photoelectrons, which are affected by the structure of the photoelectrode.[57] Although Cell-4 has the higher light harvesting 50 efficiency, the low lower IPCE value, compared with Cell-3, may be caused by the loss of photoelectron collection efficiency.

The massive charge recombination, taking place dominantly at TiO$_2$/electrolyte, QDs/electrolyte and FTO/electrolyte interfaces, are considered as an important source for the low *PCE* of 55 QDSSCs. In order to shed light on the electron recombination dynamics, the QDSSCs were tested by the transient photovoltage measurement. At the open circuit condition, the free photoelectrons injected in the conduction band of the TiO$_2$ would all recombine with the redox spices at the aforementioned three 60 interfaces, resulting in an exponential decay of the photovoltage and the *in situ* electron recombination lifetime (τ_r) is therefore estimated by the exponential fitting of the photovoltage transient decay curves.[58] **Fig. 8** depicts the τ_r obtained at different bias voltages. The bias voltage was induced by applying steady 65 illumination on the cells, which could fill electrons into the energy states of TiO$_2$ with stepwise sequence from deep traps, shallow traps to the conduction band. As increasing the bias voltage, more trap states were filled and the pulse illumination generated photoelectrons are injected into the higher energy 70 levels, which induces a faster recombination as the pulse illumination is removed. Therefore, the as-obtained τ_r value experiences a decreasing trend as increasing the bias voltage, which is in accord with the previous reports.[59,60] As mixing PMSs into the film structure (Cell-2), the τ_r is generally increased 75 compared with that of nanocrystal cell (Cell-1). The primary nanoparticles consisted in the PMSs are closely linked compared with the individual nanoparticles, which could help to decrease the number of grain boundaries, minimize the density of the trap states and reduce the recombination opportunities. Meanwhile, 80 Cell-3 has a greater τ_r than that of Cell-4 deriving
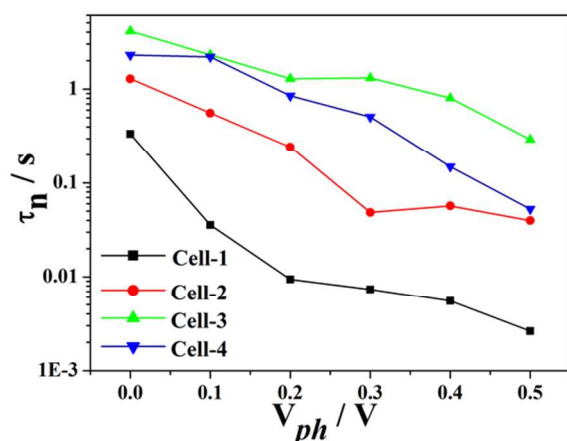
Fig. 8 the electron recombination lifetime of the four cells in function of the applied voltages obtained from the transient photovoltage (TPV) measurements.

5 from pure PMSs photoanode, implying that the recombination between the injected photoelectrons and the electron acceptors in bilayer photoanode is effectively retarded. Although the Film-4 has higher QDs loading amount and better light scattering effect, the Achilles' heel is that the packing of the submicron sized
10 PHMs usually leaves a portion of the FTO surface uncovered.[61] For the bilayer cell, the firstly deposited nanoparticles in the bilayer film give a better coverage of the FTO and alleviate the electron leaking at the FTO/electrolyte interface, which contributed to the higher τ_r in Cell-3.
15 In addition, the V_{oc} of the QDSSC device could be expressed as:[54]

$$V_{oc} = \frac{RT}{\beta F} ln\left(\frac{AI}{n_0 k_b \left[S_n^- \right] + n_0 k_r \left[D^+ \right]} \right) \quad \text{(Eqn. 2)}$$

where R is the molar gas constant, T the temperature, β the reaction order of S_n^- and electrons, F the Faraday constant, A the
20 electrode surface area for light absorption, I the incident photon flux, n_0 the accessible electronic state concentration in the conduction band, k_b the backward reaction kinetic constant of the injected electrons with polysulfide electrolyte and k_r the recombination kinetic constant of the electrons with oxidized
25 QDs (D^+). At a given I, the high light harvesting grate would increase the electron concentration in the TiO$_2$ conduction band. Moreover, the suppressed recombination of the charge carriers reduced the values of k_b and k_r, which finally results in the higher V_{oc} of Cell-3.
30 The electron collection time (τ_{col}) was test by transient photocurrent measurement (TPC). As removing the pulse illumination, the cells are switched to short circuit condition and the external circuit is series connected with a 50 ohme resistor which is shunted with a voltmeter. Therefore, the photo-separated
35 electrons and holes would transport through the out circuit, and the fading of photocurrent could be monitored by the voltage decay obtained from the voltmeter. [62] **Fig. 9** displays the collection time (τ_{col}) of the photoelectron in function of bias voltages. It is evident that Cell-3 has the lowest τ_{col} at the whole
40 bias voltage range, indicating the photoelectrons could be more effectively transported in the film structure and collected by the substrate compared with the other cells. According to Eqn. 3,[63]

$$D_e = d^2/2.35\tau_{col} \quad \text{(Eqn. 3)}$$

the electron diffusion coefficient (De) could be calculated, where
45 d is the film thickness and τ_{col} is collection lifetime obtained as the no bias voltage was applied (0 V). As a result, Cell-4 shows a
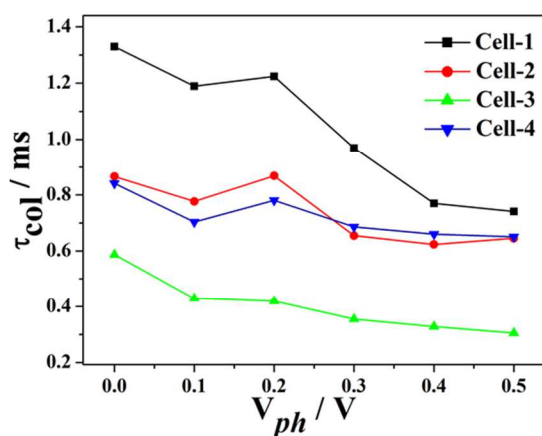

Fig. 9 The electron collection time obtained from the transient photocurrent (TPC) measurements for the four QDSSCs in
50 function of the applied voltages.

high De of 142.0×10^{-9} m^2 s^{-1}, while the De of Cell-1, Cell-2 and Cell-3 respectively reach to 62.7×10^{-9}, 96.3×10^{-9} and 99.1×10^{-9} m^2 s^{-1}. For Cell-1, great amount of grain boundaries and surface defect are existed in the nanoparticle based film, which would
55 slow down the electron hopping from the generating sites to the FTO collector and lead to lower De. As it is indicated in previous works, the introduction of PMSs with interconnect primary particles could lead to better electron diffusion.[47,61] However, the paradox situation is the electron transport among the individual
60 PMSs is retarded due to the insufficient physical contact of the adjacent PMSs.[64] Therefore, the De of Cell-2 and Cell-3 was slightly increased. Difference from the DSSC system, in spite of the TiO$_2$ matrix, the inter-connected semiconducting QDs could also sever as the electron transport pathway. Therefore, the high
65 QDs loading amount may also help to improve the intrinsic diffusion coefficient of the photoanode structure. It could be concluded that the bilayer photoanode could well integrate the structural advantages of nanocrystals and PMSs to achieve a compromise between the QDs loading and the intrinsic TiO$_2$
70 scaffold network, which results in an improved electron diffusion coefficient.

Conclusions

In summary, TiO$_2$ polydisperse mesoporous spheres and nanocrystal were intentionally prepared to investigate the effect
75 of the photoanode structure over the performance of QDSSCs. Based on the optical and photoelectric investigation, it was found that the bilayer cell possesses the priority to promote the harvesting of incident light by increasing the QDs loading amount and scattering effect. According to the transient
80 photoelectron dynamic investigation, in the bilayer QDSSC, the carrier recombination at the TiO$_2$/electrolyte and FTO/electrolyte interfaces were substantially passivated. Moreover, an electron diffusion coefficient of 142.0×10^{-9} m^2 s^{-1} was also obtained in the bilayer cell, which almost triples the value of normally used
85 nanoparticle cell, indicating the photoelectrons could be effectively transported and collected. Therefore, the bilayer photoanode could well integrate the structural advantages of the nanocrystal and the PMSs, which finally balance the requirements of QDs loading amount, scattering effect, electron
90 recombination and transport and lead to a high conversion efficiency of 4.70%, indicating a ~54% and ~12% improvement compared with the cells respectively derived from nanocrystal and PMSs.

Acknowledgements

Notes and references

[a] *Beijing National Laboratory for Molecular Sciences, State Key Laboratory for Structural Chemistry of Unstable and Stable Species, College of Chemistry and Molecular Engineering, Peking University, Beijing 100871, P.R. China, Tel./Fax: 86-10-62760360, E-mail: dsxu@pku.edu.cn*

[b] *School of Chemistry and Chemical Engineering, Henan Normal University, Henan Xinxiang 453007, P.R. China, Tel./Fax: 86-37-3326209, E-mail address: jiangkai6898@126.com*

[c] *Department of Chemistry, Renmin University of China, Beijing 100872, P. R. China, Tel./Fax: 86-10-62511528,*

E-mail address:xcai@chem.ruc.edu.cn

† Electronic Supplementary Information (ESI) available: [details of the SEM and XRD characterization of the intermediate product and the anataase nanocrystals]. See DOI: 10.1039/b000000x/

References

1   B. O'Regan, M. Gratzel, *Nature*, 1991, 353, 737-740.
2   M. Gratzel, *Nature*, 2001,414,338-344.
3   M.Gratzel, *Inorg. Chem.*, 2005, 44, 6841-6851.
4   A. Yella, H.W. Lee, H.N. Tsao, C. Yi, A.K. Chandiran, M.K. Nazeeruddin, E.W.G. Diau, C.Y. Yeh, S.M. Zakeeruddin, M. Gratzel, *Science*, 2011, **334**, 629-634.
5   S. Mathew, A. Yella, P. Gao, R. Humphry-baker, B. Curchod, N. AshariAstani, I. Tavernelli, U. Rothlisberger, M.K. Nazeeruddin, M. Grätzel, *Nat. Chem.*, 2014, 6, 242–247.
6   P.V. Kamat, *J. Phys. Chem. C*, 2008,112 , 18737-18753.
7   Y.L. Lee, Y.S. Lo, *Adv. Funct. Mater.*,2009,19, 604-609.
8   J. Lee, D. Son, T. Ahn, H. Shin, I. Kim, S. Hwang, M. Ko, S. Sul, H. Han, N. Park, *Sci. Reports*, 2013, 3, 1050.
9   P.K. Santra, P.V. Kamat, *J. Am. Chem. Soc.*, 2012, 134 ,2508-2511.
10   H. McDaniel, N. Fuke, N. Makarov, J. Pietryga, V. Klimov, *Nat. Comm.*, 2013, 4, 2887.
11   W.W. Yu, L.H. Qu, W.Z. Guo, X.G. Peng, *Chem. Mater.*, 2003, 15, 2854–2860.
12   P. Wang, S.M. Zakeeruddin, J.E. Moser, R. Humphry-Baker, P. Comte, V. Aranyos, A. Hagfeldt, M.K.Nazeeruddin, M. Grätzel, *Adv. Mater.*, 2004, 16, 1806–1811.
13   B.Qin, H. Chen, H. Liang, L. Fu, X. Liu, X. Qiu, S. Liu, R. Song, Z.Y. Tang, *J. Am. Chem. Soc.*, 2010, 132, 2886–2888.
14   X. Liu, Y. Gao, X. Wang, S.Wu, Z.Y. Tang, *J. Nanosci. Nanotech.*, 2011,11, 1941-1949.
15   J.B.Sambur, T. Novet, B.A. Parkinson, *Science* , 2010, 330, 63–66.
16   V.I. Klimov, *J. Phys. Chem. B*, 2006, 110, 16827–16845.
17   M.C. Hanna,A.J. Nozik, *J. Appl. Phys.*,2006, 100, 074510.
18   W. Shockley, H.J. Queisser, *J. Appl. Phys.*, 1961, 32, 510.
19   P.K. Santra, P.V. Kamat, *J. Am. Chem. Soc.*, 2013, 135, 877−885.
20   S. Moon, Y. Itzhaik, J. Yum, S. Zakeeruddin, G. Hodes, M. Grätzel, *J. Phys. Chem. Lett.*, 2010, 1, 1524–1527.
21   M. Samadpour, S. Gimenez, P. P. Boix, Q. Shen, M. E. Calvo, N. Taghavinia, A. I. zad, T. Toyoda, H. Mıguez and I. Mora-Sero, *Electrochim. Acta*, 2012, 75, 139–147.
22   T. Shu, Z. Zhou, H. Wang, G. Liu, P. Xiang, Y. Rong, H. Han and Y. Zhao, *J. Mater. Chem.*, 2012,22, 10525-10529.
23   Z. Yang, H. Chang, *Sol. Energy Mater. Sol. Cells*, 2010, 94, 2046–2051.
24   P. Sheng, W. Li, J. Cai, X. Wang, X. Tong, Q. Cai, C. Grimes, *J. Mater. Chem. A*, 2013,1, 7806-7815
25   Thomas P. Brennan, Orlando Trejo, Katherine E. Roelofs, John Xu, Fritz B. Prinz and Stacey F. Bent, *J. Mater. Chem. A*, 2013,1, 7566-7571.
26   L. Tao, Y. Xiong, H. Liu and W. Shen, *Nanoscale*, 2014, 6, 931-938
27   H. Shen, X. Jiao, D. Oron, J. Li, H. Lin, *J. Power Sources*, 2013, 240, 8-13.
28   H. Choi, I. Ji, J. Bang, *ACS Appl. Mater. Interfaces*, 2014, 6, 2335-2343.
29   H. Zhang, Y. Li, Y. Wang, P. Liu, H. Yang, X. Yao, T. An, B. Wood and H. Zhao, *J. Mater. Chem. A*, 2013,1, 6563-6571.
30   K. Meng, P. Surolia and R. Thampi, *J. Mater. Chem. A*, 2014, Accepted Manuscript (DOI: 10.1039/C4TA00877D).
31   J. Xiao, Q. Huang, J. Xu, C. Li, G. Chen, Y. Luo, D. Li, and Q. Meng, *J. Phys. Chem. C*, 2014, 118, 4007-4015.
32   Z. Zhu, J. Qiu, K. Yan, S. Yang, *ACS Appl. Mater. Interfaces*, 2013, 5, 4000-4005.
33   C. Shen, L., Z. Koh, Q. Wang, *J. Mater. Chem. A*, 2014,2, 2807-2813.
34   C. Lin, C. Teng, T. Li, Y. Lee and H. Teng, *J. Mater. Chem. A*, 2013,1, 1155-1162 .
35   C. Chang, J. Chen, C. Chen, C. Yang, J. Chang, *ACS Appl. Mater. Interfaces*, 2013, 5, 11296-11306.
36   H. Choi, C. Nahm, J. Kim, C. Kim, S. Kang, T. Hwang, B. Park, *Curr. Appl. Phys.*, 2013, 13, S2-S13.
37   D. A. Hines, P. V. Kamat, *ACS Appl. Mater. Interfaces*, 2014, 6, 3041-3057.
38   Q.X. Zhang, X.Z. Guo, X.M. Huang, S.Q. Huang, D.M. Li, Y.H. Luo, Q. Shen, T. Toyoda, Q. Meng, *Phys. Chem. Chem. Phys.*, 2011, 13, 4659-4667.
39   J. He, D.Wu, Z. Gao, F.Xu, S. Jiang, S. Zhang, K. Cao, Y. Guo, K.Jiang, *RSC Adv.*, 2014,4, 2068-2072
40   H. Zhang, K. Cheng, Y.M. Hou, Z. Fang, Z.X. Pan, W.J. Wu, J.L. Hua, X. H. Zhong, *Chem. Commun.*, 2012, 48, 11235-11237.
41   K. Yan, W. Chen, S. Yang, *J. Phys. Chem. C*, 2013, 117, 92−99.
42   I. Mora-Sero, J. Bisquert, *J. Phys. Chem. Lett.*, 2010, 1, 3046–3052.
43   M. Shalom, S. Buhbut, S. Tirosh, A. Zaban, *J. Phys. Chem. Lett.*, 2012, 3, 2436−2441.
44   H. Wang, M. Miyauchi, Y. Ishikawa, A. Pyatenko, N. Koshizaki, Y. Li, L. Li, X. Li, Y. Bando, D. Golberg, *J. Am. Chem. Soc.*, 2011, 133, 19102–19109.
45   Q. Zhang, T. P. Chou, B. Russo, S. A. Jenekhe and G. Z. Cao, Adv. Funct. Mater., 2008, 18, 1654-1660.
46   Y. J. Kim, M. H. Lee, H. J. Kim, G. Lim, Y. S. Choi, N.-G. Park, K. Kim and W. I. Lee, Adv. Mater., 2009, 21, 3668–3673.
47   W.G. Yang, F.R. Wan, Q.W. Chen, J.J. Li, D.S. Xu, *J. Mater. Chem.*, 2010, 20, 2870–2876.
48   D.H. Chen, F.Z. Huang, R.A. Caruso, Y.B. Cheng, *Adv. Mater.*, 2009, 21, 2206-2210.
49   J. Li, Y. Yu, Q. Chen, J. Li, D. Xu, *Cryst. Growth Des.*, 2010, 10, 2111–2115.
50   D. Wu, F. Zhu, J. Li, H. Dong, Q. Li, K. Jiang, D. Xu, *J. Mater. Chem.*, 2012, 22, 11665-11671.
51   J.G. Yu, J. Zhang, *Dalton Trans.*, 2010, 39, 5860-5867.
52   D.P. Wu, Z.Y. Gao, F. Xu, J.L. Chang, W.G. Tao, J.J. He, S.Y. Gao, K. Jiang, *CrystEngComm*, 2013,15, 1210-1217.
53   X. Yu, J. Liao, K. Qiu, D. Kuang, C. Su, *ACS Nano*, 2011, 5, 9494–9500.
54   F. Zhu, H. Dong, Y. Wang, D. Wu, J. Li, J. Pan, Q. Li, X. Ai, J. Zhang and D. Xu, *Phys. Chem. Chem. Phys.*, 2013,15, 17798-17803.
55   J. J. Tian, R. Gao, Q. F. Zhang, S. G. Zhang, Y. W. Li, J. L. Lan, X. H. Qu and G. Z. Cao, *J. Phys. Chem. C*, 2012, 116, 18655−18662.
56   R. Zhou, Q. Zhang, E. Uchaker, J. Lan, M. Yin and G. Cao, *J. Mater. Chem. A*, 2014, 2, 2517–2525.
57   J. Bisquert, A. Zaban, M. Greenshtein, I. Mora-Sero, *J. Am. Chem. Soc.*, 2004, 126, 13550-13559.
58   I. Mora-Sero, S. Gimenez, F. Santiago, R. Gomez, Q. Shen, T. Toyoda, J. Bisquert, *Accounts Chem. Res.* 2009, 11, 1848-1857.
59   K. Lee, S.W. Park, M.J. Ko, K. Kim, N.G. Park, *Nat. Mater.*, 2009, 8, 665–671.
60   J. Tian, Q. Zhang, E. Uchaker, Z. Liang, R. Gao, X. Qu, S. Zhang, G. Cao, *J. Mater. Chem. A*, 2013, 1, 6770–6775.

61   F. Zhu, D. Wu, Q. Li, H. Dong, J. Li, K. Jiang and D. Xu, *RSC Adv.*, 2012,2, 11629-11637

62   D.P. Wu, Y. Wang, H. Dong, F. Zhu, S.Y. Gao, K. Jiang, L.M. Fu, J.P. Zhang , D.S. Xu, *Nanoscale*, 2013, 5, 324-330.

5 63   J. Lagemaat, A.J. Frank, *J. Phys. Chem. B*, 2001, 105, 11194-11205.

64   Y. J. Kim, M. H. Lee, H. J. Kim, G. Lim, Y. S. Choi, N.-G. Park, K. Kim and W. I. Lee, *Adv. Mater.*, 2009, 21, 3668–3673.

Journal of Materials Chemistry A Accepted Manuscript